Thermocapillary effect on the dynamics of viscous beads on vertical fiber

Rong Liu[*] and Qiu Sheng Liu[†]

*Key Laboratory of Microgravity (National Microgravity Laboratory), Institute of Mechanics, Chinese Academy of Sciences,
Beijing, China 100190*

The gravity-driven flow of a thin liquid film down a uniformly heated vertical fiber is considered. This is an unstable open flow that exhibits rich dynamics including the formation of droplets, or beads, driven by a Rayleigh-Plateau mechanism modified by the presence of gravity as well as the variation of surface tension induced by temperature disturbance at the interface. A linear stability analysis and a nonlinear simulation are performed to investigate the dynamic of axisymmetric disturbances. The results showed that the Marangoni instability and the Rayleigh-Plateau instability reinforce each other. With the increase of the thermocapillary effect, the fiber flow has a tendency to break up into smaller droplets.

I. INTRODUCTION

A liquid film flowing down a vertical fiber has been extensively studied recently because it is encountered in many industrial applications, for example, draining, coating of insulation on a wire, and the protection coating of tube walls [1]. For cylindrical threads and jets, a Rayleigh-Plateau mechanism is responsible for the formation of very regular droplike wave patterns under the action of surface tension [2]. For the film of thickness h flowing down a slender cylindrical fiber of radius a, the Rayleigh-Plateau instability is modified by the presence of flow driven by gravity. Surface tension acts to destabilize the interface by the Rayleigh mechanism. At small Reynolds numbers, the film tends to break up into axisymmetric droplets with the axial length scale $\mathcal{L} > 2\pi R$, here $R = a + h$ is the total radius of the fluid ring.

Experimental investigation on the thin films flowing down a vertical fiber was performed first by Quéré [3]. The results showed that two different kinds of behavior can be observed according to the film thickness: (1) For a thick film on a slender fiber, drops develop due to the Rayleigh instability and flow downward. Some of drops grow by swallowing the other ones, and quickly fall, leaving behind them a thick film which breaks in turn into droplets. (2) For a thin film on a large fiber, the instability may be arrested by the mean flow.

Frenkel has derived a simple Benny-like equations for the evolution of the film thickness in the case of $h \ll a$ [4]. Kalliadasis and Chang [5] solved the evolution equation derived by Frenkel [4] and showed that the mean flow can arrest the drop formation process when the thickness of the film is less than the critical value, h_c, observed by Quéré [3] in which $h_c \sim a^3 H^{-2}$, where $H = (\sigma/\rho g)^{1/2}$. The nonlinear dynamics of Frenkel's equation has also been investigated by Kerchman and Frenkel [6] and Chang and Demekhin [7].

The above papers deal with the long-wave equations derived under the assumption that the fiber radius is taken to be much

larger than the film thickness. Kliakhandler *et al.* [8] conducted experiments that revealed the richness of the dynamics of the flow of a thick film down a vertical fiber. Three qualitatively different regimes of the interfacial patterns in the form of beads were observed experimentally. The photos of three distinct regimes (a), (b), and (c) reported by Kliakhandler *et al.* in Fig. 1 in Ref. [8]. In the first case of flow regime (a), the drops are large and move rapidly and the flow rates are relatively large. The film between the drops is relatively thick and practically uniform. The average distance between the drops is relatively large, though the separation between the individual drops slightly varies. The large drops sometimes collide very quickly with each other in an irregular fashion. In the second case of flow regime (b), the drop train is highly organized. The speed and size of the drops are substantially smaller than those in regime (a), and the shape, speed, and distance between the drops do not change over time. This regime was observed in a relatively small range of flow rates. For very small flow rates, the size and speed of the drops in regime (c) are larger than those in regime (b), though the flow rate in regime (c) is smaller. Regime (c) is also not steady as the large drop is actually consuming the much smaller stationary drop ahead in the experiments.

In the experiments in Ref. [8], the film is at least twice as thick as the fiber radius. Therefore, the previously derived Benny-like equations under the assumption of $h \ll a$ do not apply there. The authors also proposed an evolution equation which does not rely on the previously made lubrication-type assumptions. Two typical regimes at relatively small flow rate are described well by their model. However, their model equation fails to capture a regime that features beads separated by relatively long flat thin-film regions. Craster and Matar [9] derived a new evolution equation similar to that used by Kliakhandler *et al.* [8] and revisited the same problem in which the fluid radius is much smaller than its characteristic length based upon a capillary length scale. The authors showed that numerical solutions of their model equation yield good agreement with the experimental observations reported by Kliakhandler *et al.* [8]. Until now, this long-wave model has been extended to study the dynamics of the fiber flow in more complex physical conditions. Ding and Liu [10] studied the dynamics of a viscous film flowing on a porous

---
[*]liurong@imech.ac.cn
[†]liu@imech.ac.cn

cylinder. More recently, Ding *et al.* [11] investigated the effect of radial electric field on the dynamics of the fiber flow.

In many practical situations, fiber-coating processes are operated in a cooling environment. For example, in glass-manufacturing process, glass fibers are made by drawing molten glass through an array of small diameter bushings. The cooling of the fibers from the glass extrusion temperature (1500 K) to a temperature where the coating can be applied (below 365 K) is a rate-limiting step. In order to enhance the heat removal from the fibers, the fiber is sprayed with water from atomizing nozzles [12]. In the situation where the fiber flow is cooled by the environment, the capillary instability is modified by fluid motions induced by gravity as well as by thermocapillary stress, which is due to surface tension variations produced by temperature gradients.

For a planar liquid film bounded by a heated wall, two mechanisms that are associated with the thermocapillary forces can lead to instabilities [13]. One mechanism (the *P* mode) is associated with the interaction of the basic temperature with the perturbation velocity field. Upon the onset of instability, the *P* mode is in the form of static convection cells with the wavelength of the same order as the layer depth. This type of instability is first observed by Bénard [14] in thin liquid layers ($\approx$1 mm deep) heated from below. Block [15] first recognized that surface tension, instead of buoyancy, was the source of instability. Pearson [16] performed a linear stability analysis on this problem and found that this type of instability can occur in a liquid layer without surface deformation. The second mechanism is associated with the modification of the basic temperature at the free surface by the surface deformation. This long-wavelength instability mode (the *S* mode) was first predicted and investigated theoretically by Scriven and Sternling [17] and Smith [18]. VanHook *et al.* [19,20] investigated both experimentally and theoretically on the long-wave instability of a thin liquid layer heated from below or cooled from above. In the experiments, the long-wave instability mode takes the form of a localized depression ("dry spot") or a localized elevation ("high spot"), depending on the thickness and thermal conductivity of the gas layer above the liquid.

The above works in the preceding paragraph on the stability problem of surface-tension-driven flow are limited to liquid layers bounded by a plane plate. However, a careful look at previous literatures indicates that the studies on the effect of thermocapillarity on liquid flows with an axisymmetric free surface, such as jet, liquid bridge, and fiber flows, are very limited. Xu and Davis [21] have studied the stability of long axisymmetric liquid zones subjected to axial temperature gradients which induce steady flows driven by thermocapillarity. Chen *et al.* [22] have studied the effect of thermocapillarity on the Plateau-Rayleigh instability of a cylindrical liquid bridge. It has been shown that the thermocapillarity induced by axial temperature gradients has a stabilizing effect [21,22].

In the present paper, we will study the problem of a film flowing down a vertical fiber with a temperature difference between the fiber wall and the interface, which is different from Refs. [21] and [22] where the temperature gradients are parallel to the axial direction. In our problem, most of the physical parameters are the same with those of experiments by Kliakhandler *et al.* [8]. In their experiments, caster oil has the density $\rho = 0.961$ g cm^{-3}, kinematic viscosity $\nu = 4.4$ cm^2 s^{-1}, and surface tension $\sigma = 31$ g s^{-2}, and the radius of the fiber $a = 0.25$ mm. We assume that the environment is at a room temperature of $T_0 = 25^\circ$ C, and the temperature difference between the fiber wall and the fluid interface does not exceed 100° C.

This paper is organized as follows. In Sec. II the mathematical formulation of the physical model is presented. In Sec. III we present the results and discussions. In Sec. IV we summarize the results and present the conclusions.

II. MATHEMATICAL FORMULATION

As shown in Fig. 1, a Newtonian fluid, of constant viscosity μ and density ρ, flows down a vertical fiber of radius $r = a$ under gravity g. The initial radius of the fluid ring measured from the center of the fiber is $r = R$. The temperatures of the fiber wall and the interface of the film are T_a and T_i. We make an assumption that the flow is axisymmetric.

The dynamics of the flow are governed by the continuity equation, Navier-Stokes equations and the energy equation

$$u_r + \frac{u}{r} + w_z = 0, \tag{1}$$

$$u_t + uu_r + wu_z = -\frac{p_r}{\rho} + \frac{\mu}{\rho}\left[u_{rr} + \frac{u_r}{r} - \frac{u}{r^2} + u_{zz}\right], \tag{2}$$

$$w_t + uw_r + ww_z = g - \frac{p_z}{\rho} + \frac{\mu}{\rho}\left[w_{rr} + \frac{w_r}{r} + w_{zz}\right], \tag{3}$$
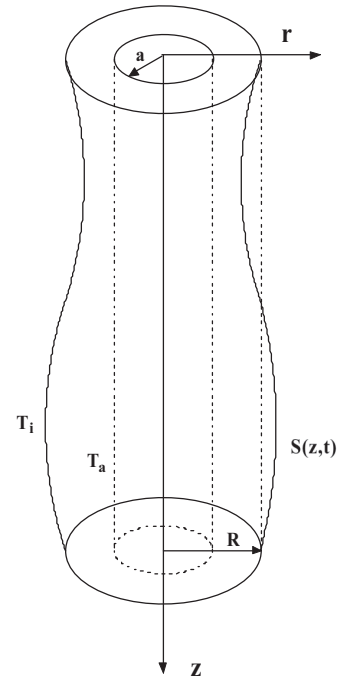

FIG. 1. Sketch of the geometry of a fiber flow.

$$T_t + uT_r + wT_z = \kappa \left[T_{rr} + \frac{T_r}{r} + T_{zz} \right], \qquad (4)$$

where t denotes time, u and w denote the radial (r) and axial (z) velocity components, p denotes the pressure, T denotes the temperature, and κ denotes the thermal diffusivity. Note that unless stated otherwise, the subscript denotes partial differentiation.

At the fiber surface ($r = a$), no penetration and no slip conditions for the velocities are

$$u = w = 0. \qquad (5)$$

The temperature at the fiber wall is prescribed:

$$T = T_a. \qquad (6)$$

At the free surface $r = S(z,t)$, the shear stress is balanced by the thermocapillary force,

$$\boldsymbol{t} \cdot \boldsymbol{T} \cdot \boldsymbol{n} = \boldsymbol{t} \cdot \nabla_s \sigma, \qquad (7)$$

and the normal stress is balanced by surface tension times the curvature,

$$\boldsymbol{n} \cdot \boldsymbol{T} \cdot \boldsymbol{n} = 2\sigma H, \qquad (8)$$

here $\boldsymbol{T}$ is the stress tensor, $\boldsymbol{n}$ and $\boldsymbol{t}$ are the unit vectors normal and tangent to the interface, and $2H$ is the surface mean curvature. The surface tension is assumed to be given by the linear dependence on the temperature,

$$\sigma = \sigma_0 - \gamma(T_i - T_0), \qquad (9)$$

where the coefficient γ represents the rate of change of surface tension with temperature, evaluated at the reference temperature T_0. This assumption is valid when the temperature difference between T_i and T_0 is not large. For most of liquid interface the surface tension decreases with temperature. For silicone oil at $25°$ C, the coefficient γ is about 0.5×10^{-4}.

In component form, Eqs. (7) and (8) can be expressed as

$$\frac{\mu}{N} \left[2S_z(u_r - w_z) + (1 - S_z^2)(w_r + u_z) \right] = -\gamma(S_z T_{ir} + T_{iz}), \qquad (10)$$

$$p + \frac{2\mu}{N^2} \left[S_z(u_z + w_r) - u_r - S_z^2 w_z \right] = \sigma \left(\frac{1}{NS} - \frac{S_{zz}}{N^3} \right), \qquad (11)$$

where $N = (1 + S_z^2)^{1/2}$.

The kinematic boundary condition on the free surface is

$$S_t + wS_z - u = 0, \qquad (12)$$

or in conservative form

$$S_t + \frac{1}{S} \frac{\partial}{\partial z} \int_a^S wr \,\mathrm{d}r = 0. \qquad (13)$$

The balance between heat supply to and heat loss from the surface is given by a phenomenological relation referred as

"Newton's law of cooling,"

$$-\chi \boldsymbol{n} \cdot \nabla T = q(T - T_\infty), \qquad (14)$$

in which χ is the thermal conductivity of the liquid and q is the Newton's heat transfer coefficient describing the rate of heat transport from the liquid to the ambient gas with temperature T_∞ far away from the interface. This law, which is often applied in the absence of radiation, is not a rigorous condition expressing energy conservation through the interface, with a value of q determined empirically. This relation is not valid when the boundary possesses a non-negligible thermal resistance. Moreover, it may not be adequate in describing cooling due to convection in the gas phase [23].

Scaling and asymptotic reduction

The dimensionless variables are

$$r = Rr^*, \quad z = Lz^*, \quad p = \rho gLp^*, \quad t = LV^{-1}t^*, \\ w = Vw^*, \quad u = \epsilon Vu^*, \quad T - T_\infty = \Delta T T^*, \qquad (15)$$

where the star denotes dimensionless variables, and the velocity scale $V \equiv \rho g R^2/\mu$. The length scale L is taken to be the capillary length $L = \sigma/\rho gR$. We assume that the radius of the fluid ring, R, is much smaller than the length scale L, i.e., the parameter $\epsilon = R/L$ is small. The Bond number Bo $= \rho g R^2/\sigma$ naturally appears and in the experiments the Bond number is small (~ 0.3 or so) [9]. This quantity indicates the dominating effect of gravity over surface tension. Note that the choice of length scale above sets Bo $= \epsilon$. This means that the choice of a low Bond number (surface-tension-dominated) is consistent with the long-wave theory. We drop the star and exclusively use dimensionless variables throughout the subsequent parts of the present paper.

The dimensionless controlling equations become

$$u_r + \frac{u}{r} + w_z = 0, \qquad (16)$$

$$\epsilon^4 \mathrm{Re}(u_t + uu_r + wu_z) = -p_r + \epsilon^2 \left[u_{rr} + \frac{u_r}{r} - \frac{u}{r^2} + \epsilon^2 \frac{\partial^2 u}{\partial z^2} \right], \qquad (17)$$

$$\epsilon^2 \mathrm{Re}(w_t + uw_r + ww_z) = 1 - p_z + \left[w_{rr} + \frac{w_r}{r} + \epsilon^2 w_{zz} \right]. \qquad (18)$$

$$\epsilon^2 \mathrm{Re}(T_t + uT_r + wT_z) = \frac{1}{\mathrm{Pr}} \left[T_{rr} + \frac{T_r}{r} + \epsilon^2 T_{zz} \right], \qquad (19)$$

where the Reynolds number is defined as Re $= \rho VL/\mu$, and the Prandtl number is defined as Pr $= \nu/\kappa$. Assuming $\epsilon^2 \ll 1$ and Re $= O(1)$ or smaller, we can neglect the contributions of the inertial terms.

The leading-order Navier-Stokes equation and the energy equation are given by

$$w_{rr} + \frac{w_r}{r} = p_z - 1, \qquad (20)$$

$$T_{rr} + \frac{T_r}{r} = 0. \qquad (21)$$

The leading-order normal and tangential stress balances at the surface are

$$p = \frac{1}{S} - \epsilon^2 S_{zz}, \tag{22}$$

$$w_r = -\epsilon \mathrm{Ma}(S_z T_{ir} + T_{iz}), \tag{23}$$

where the Marangoni number is defined as $\mathrm{Ma} = \gamma \Delta T / \mu V$. The parameter Ma measures the importance of the tangential thermocaillary stresses at the free surface.

A notable term which is included in Eq. (22) is the ϵS_{zz} term, which involves the highest derivative of S. Strictly speaking, the inclusion of this term may appear to be *ad hoc*. A singular perturbation suggests that the S_{zz} term should be important. This is reflected in a linear analysis where the inclusion of this term is vital to ensure the correct cutoff wave number. More justification of inclusion of this term has been reviewed by Craster and Matar [9]. In Eq. (23), the reason for including the first order term of ϵ is that the Marangoni effect is involved in this term.

The temperature at $r = a$ is

$$T = 1, \tag{24}$$

the relation of Newton's law of cooling at the surface $r = S$

$$T_r + \mathrm{Bi}T = 0, \tag{25}$$

where the Biot number defined as $\mathrm{Bi} = qR/\chi$ measures the efficiency of heat transfer at the boundary. $\mathrm{Bi} = 0$ corresponds to the poorly conducting case, while $\mathrm{Bi} \to \infty$ corresponds to a perfectly conducting case.

We obtain the distribution of the temperature as

$$T = \frac{\mathrm{Bi}\ln\frac{r}{S} - \frac{1}{S}}{\mathrm{Bi}\ln\frac{a}{S} - \frac{1}{S}}. \tag{26}$$

At the interface, the temperature is

$$T_i(z) = \frac{-1}{\mathrm{Bi}S\ln\frac{a}{S} - 1}. \tag{27}$$

The velocity $w(r,z,t)$ is

$$w = (1 - p_z)\left[\frac{1}{4}(a^2 - r^2) + \frac{1}{2}S^2 \ln\frac{r}{a}\right] - \epsilon \mathrm{Ma}T_{iz}S \ln\frac{r}{a}. \tag{28}$$

Substituting w to the continuity equation, we obtain the expression of u,

$$u = -\frac{1}{r}\left\{A_z\left[\frac{1}{2}a^2(r^2 - a^2) - \frac{1}{4}(r^4 - a^4)\right] + B_z\left[\frac{1}{2}r^2 \ln\left(\frac{r}{a}\right) - \frac{1}{4}(r^2 - a^2)\right]\right\}, \tag{29}$$

where A and B are

$$A = \frac{1}{4}(1 - p_z), \quad B = \frac{S^2}{2}(1 - p_z) - \epsilon \mathrm{Ma}T_{iz}S, \tag{30}$$

where

$$T_{iz} = \frac{\mathrm{Bi}S_z\left(\ln\frac{a}{S} - 1\right)}{\left(\mathrm{Bi}S\ln\frac{a}{S} - 1\right)^2}. \tag{31}$$

We can define a stream function $\Psi(r)$ as

$$\Psi(r) = \int_a^r ru\,\mathrm{d}r = (1 - p_z)\left[-\frac{1}{16}(r^4 - a^4)\right.$$
$$+ \frac{1}{4}S^2 r^2 \ln\left(\frac{r}{a}\right) - \frac{1}{8}(S^2 - a^2)(r^2 - a^2)\right]$$
$$- \epsilon \mathrm{Ma}T_{iz}S\left[\frac{r^2}{2}\ln\frac{r}{a} - \frac{1}{4}(r^2 - a^2)\right], \tag{32}$$

and the flow rate $Q = \Psi|_{r=S}$ is expressed as

$$Q(S) = (1 - p_z)\left[\frac{1}{4}S^4 \log\frac{S}{a} + \frac{(3S^2 - a^2)(a^2 - S^2)}{16}\right]$$
$$- \epsilon \mathrm{Ma}T_{iz}\left[\frac{S^3}{2}\ln\frac{S}{a} - \frac{S}{4}(S^2 - a^2)\right]. \tag{33}$$

Substituting Q in the kinematic boundary condition yields an evolution equation for $S(z,t)$ given by

$$\partial_t S^2 + 2\partial_z Q(S) = 0. \tag{34}$$

III. RESULTS AND DISCUSSIONS

Throughout the present paper, the results are based on the nonlinear evolution equation (34), which is obtained from the leading order approximation with respect to ϵ. In the experiments in Ref. [8], the Reynolds number of the flow is very small, typically 10^{-2}. In this case, Eq. (34) is valid for $\epsilon^2 \ll 1$.

Before we perform a linear stability analysis on the problem, it is helpful to give a physical interpretation of the mechanisms of the Marangoni effect on the stability. We begin by analyzing the dynamics of a small disturbance at the interface of the film fiber. At the interface, crest and trough are formed due to the growth of the deflexion driven by the Rayleigh-Plateau mechanism. When the film is heated by the fiber, because the trough point is closer to the fiber wall, the temperature at the trough is higher than that at the crest. A fluctuation of temperature will result in a local surface tension gradient. Surface tension gradients at the interface act as tangential stress on adjacent fluids. The interface relaxes at the trough point where a positive temperature disturbance is created and the associated tangential stresses then induce the fluid flow from the trough towards the crest. Thus, we conjecture that the Marangoni effect and the Rayleigh-Plateau mechanism reinforce one another.

A. Linear stability

Let us now consider the linear stability of the problem. The base state of Eq. (30) is

$$\bar{S} = 1. \tag{35}$$

We use a normal mode approach

$$S = \bar{S} + \hat{S}\exp(\lambda t + ikz). \tag{36}$$

Where $\hat{S}$ is the amplitude of the perturbation, k and λ are the wave number and the time growth rate. This yields the
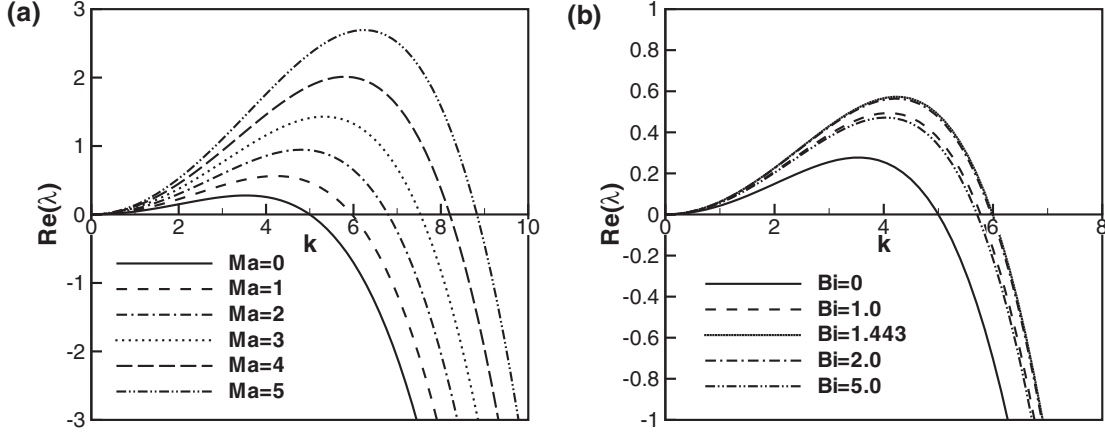
FIG. 2. The dispersion relation of the real growth rate vs the wave number. (a) For various Marangoni numbers at $Bi = 1.0$, (b) for various Biot number at $Ma = 1.0$. Other parameters are $\epsilon = 0.2$, $a = 0.5$.

dispersion relation

$$\lambda + \left[\frac{1}{16} k^2 (k^2 \epsilon^2 - 1) \left(4 \ln \frac{1}{a} - a^4 + 4a^2 - 3 \right) + \frac{ik}{2} (a^2 - 1 - 2 \ln a) \right] + \frac{\epsilon}{4} k^2 \mathrm{MaBi} \frac{(a^2 - 1 - 2 \ln a)(\ln a - 1)}{(\mathrm{Bi} \ln a - 1)^2} = 0. \quad (37)$$

At $Ma = 0$, this dispersion relation is identical to that of Craster and Matar for a fiber flow of an isothermal liquid [9]. In Fig. 2 we show the curves of the dispersion relations obtained from the long-wave theory. At a given k, it can be seen from Eq. (38) that the time-growth rate increases with the increase of Ma. The maximum real growth rate

$$\lambda_m = \frac{A}{64\epsilon^2} \left(1 + 4\epsilon \mathrm{Ma} \frac{B}{A} \right)^2 \quad (38)$$

is realized at the wave number

$$k_m = \frac{1}{\sqrt{2}\epsilon} \left(1 + 4\epsilon \mathrm{Ma} \frac{B}{A} \right)^{1/2}, \quad (39)$$

in which the coefficients A and B are

$$A = 4 \ln \frac{1}{a} - a^4 + 4a^2 - 3,$$

$$B = -\mathrm{Bi} \frac{(a^2 - 1 - 2 \ln a)(\ln a - 1)}{(\mathrm{Bi} \ln a - 1)^2}. \quad (40)$$

The cutoff wave number at which the real growth rate is zero is

$$k_c = \frac{1}{\epsilon} \left(1 + 4\epsilon \mathrm{Ma} \frac{B}{A} \right)^{1/2}. \quad (41)$$

As shown in Fig. 2(a), with the increase of the Marangoni number, both the wave number of the most unstable mode and the cutoff wave number increase.
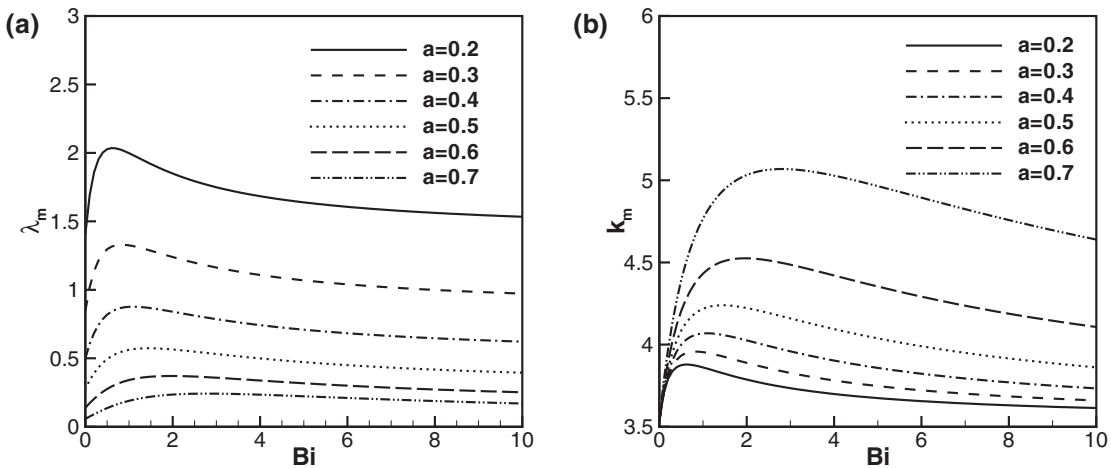

FIG. 3. Effect of Bi on the real growth rate and the wave number of the most unstable mode for various a. (a) The curves of λ_m vs Bi, (b) the curves of k_m vs Bi. The other parameters are $\epsilon = 0.2$, $Ma = 1.0$.

TABLE I. The values of α and ϵ for flow regions a, b, and c.

	a	b	c
a	0.2551	0.2856	0.3262
ϵ	0.2915	0.233	0.178

The Biot number is an important factor to influence the growth rate of disturbances. For Bi $= 0$, the interface is perfectly insulated from the gas. In that case the temperature of the film is $T = 1$. For Bi $\to \infty$, the interface is a perfect conductor, and the temperature of the interface is identical to the gas, i.e., $T_i = 0$. In these two cases, there is no temperature disturbance at the interface, and the dispersion relations are identical to the fiber flow of an isothermal liquid. It can be shown from Eq. (40) that as Bi $< 1/\ln(\frac{1}{a})$, the real time-growth rate increases with Bi, and as Bi $\geqslant 1/\ln(\frac{1}{a})$ it decreases with the increase of Bi. Figure 2(b) displays the dispersion relations for various Bi at Ma $= 1$ for $a = 0.5$. At Bi ≈ 1.443, the time-growth rates reach the maximal value at all wave numbers.

In Fig. 3(a) and 3(b), the time-growth rate and the corresponding wave number of the most unstable mode versus the Bi are plotted for various a. At each Bi, both the time-growth rate and the wave number decrease with the increase of a. For a given a, both the time-growth rate and the wave number reach their maximum values as Bi $= 1/\ln(\frac{1}{a})$.

B. Nonlinear evolution

In this subsection we will study the effect of thermocapillarity on the nonlinear evolution of small disturbances. Equation (34) subject to periodic boundary conditions will be numerically simulated. We now examine the nonlinear evolution initiated by small disturbances of the most unstable modes with wavelength $\lambda = 2\pi/k_m$. The initial condition is a simple harmonic disturbance superimposed on the interface

$$S_0 = \bar{S} + \varepsilon \cos(k_m z), \quad (42)$$

where ε is a small number. The computational domain is set to be the interval $[-\pi/k_m, \pi/k_m]$. A Fourier pseudospectral method is used to provide the discretization in space. The second-order Runge-Kutta method for stiff problems was used for the time advance.

Next, we will examine how the thermocapillarity influences the flows in these typical regimes. The parameters a and ϵ for different flow regimes are listed in Table I. In order to know the effect of thermocapillarity on the characteristics of the flow, we will examine how the Marangoni number influences the profiles of the interface of the nonlinear state.

In Fig. 4 we plot the profiles of the saturate state of the nonlinear evolution initiated by small disturbances of the most unstable modes with wavelength $\lambda = 2\pi/k_m$. At the saturate state, the evolution is in the form of a traveling wave. In these figures, the small amplitude initial disturbances give similar periodic structures at Ma $= 0$. With the increase of Ma, the hight of the beads increases and the gap between drops becomes flatter. As Ma increases to 2, the gaps between the drops become virtually uniform interfaces.

Figure 5 shows the evolution of the most unstable mode by plotting a sequence of snapshots of the free-surface profiles at fixed time increments. As shown in Fig. 5, the perturbed interface becomes unstable and the disturbance saturates with small-amplitude waves. Comparing Fig. 5(a) with Fig. 5(b), we found that at large Marangoni number Ma $= 2$ the disturbance grows more rapidly into traveling waves than at Ma $= 0$.

The saturate states of the most unstable mode are clearly families of the steadily propagating solutions. In order to know the properties of the solutions which are naturally selected, we perform numerical simulations on relatively long domains. Starting from a fiber flow of uniform radius seeded with random disturbance in the range 0 to 10^{-3} on a spatial domain of $l = 15$, the solutions are plotted in Figs. 6–8. As shown in Figs. 6(a), 7(a), and 8(a) for Ma $= 0$, the beads with similar structures coexist and the lengths of gaps between beads are different. In Figs. 6(b), 7(b), and 8(b) for Ma $= 1$, in comparison with the case of Ma $= 0$ the width of each bead decreases and more beads appear in the region. As Ma increases from 0 to 1, the height of each bead increases and the thicknesses of the gaps between different "families" decrease. As Ma increases to 2, Figs. 6(c) and 8(c) present the profiles of breakup of the film. In these two figures, a noticeably large
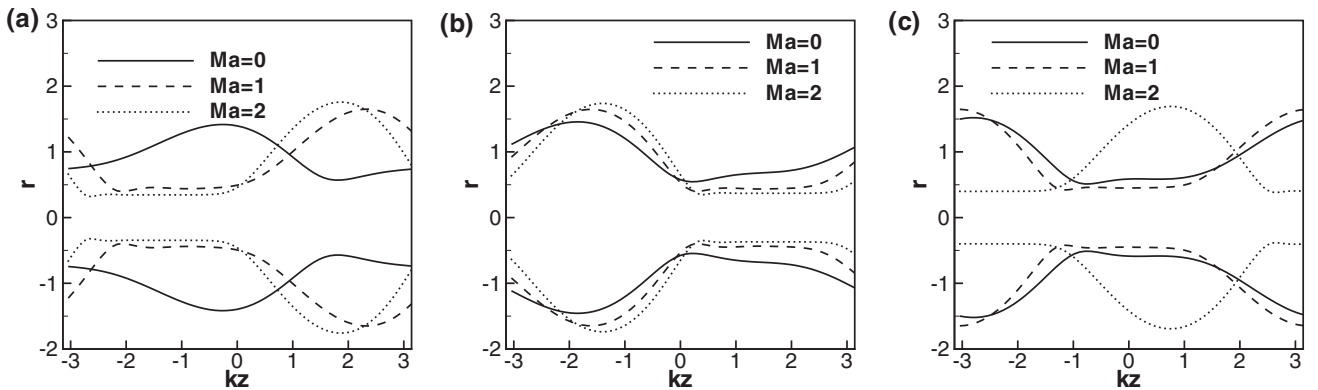

FIG. 4. Effect of Ma on the profiles of the interface via numerical simulations for the most unstable disturbances. (a), $a = 0.2551$, $\epsilon = 0.2915$, $k = 2.47, 2.78, 3.09$ for Ma $= 0, 1, 2$; (b), $a = 0.2856$, $\epsilon = 0.233$, $k = 3.09, 3.47, 3.73$ for Ma $= 0, 1, 2$; (c), $a = 0.3262$, $\epsilon = 0.178$, $k = 4.045, 4.3820, 4.8876$ for Ma $= 0, 1, 2$.
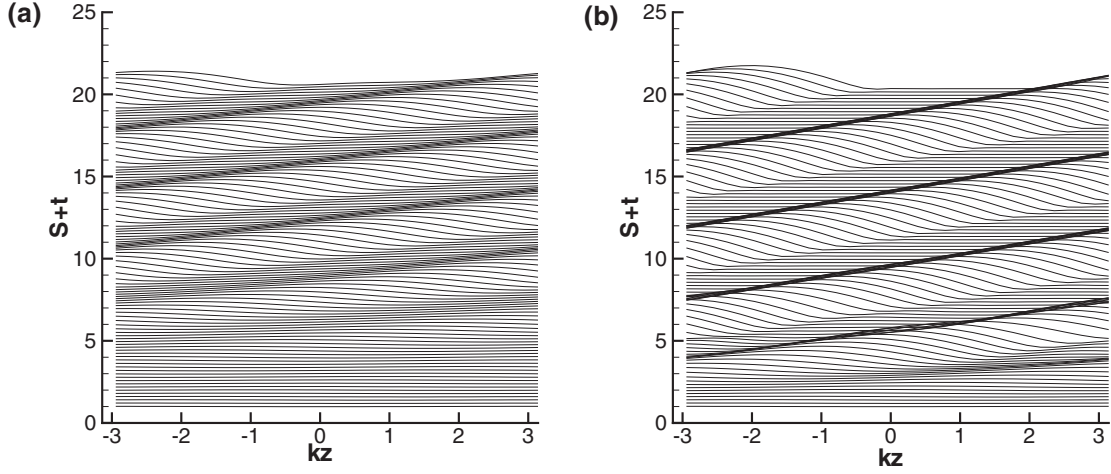
(a)

(b)

FIG. 5. Time snapshots showing the evolution of the most unstable mode in a periodic domain of $2\pi/k_m$ from $t = 0$ to 20 for $a = 0.2551$, $\epsilon = 0.2915$. Interfacial profiles S are shown at time intervals $\Delta t = 0.2$. (a) $k = 2.47$, Ma $= 0$; (b) $k = 3.09$, Ma $= 2$.

bead accompanied with a series of smaller droplets appears in the region, and the minimum thickness of the film is close to zero. In Fig. 7(c) for Ma $= 2$, the width of each bead and the thickness of the gap between different "families" decreases further. In this figure, the breakup of the film has not occurred as that shown in Figs. 6(c) and 8(c). From the discussion above, the results in Figs. 6–8 indicate that the fiber flow has a tendency to break up into smaller beads under the effect of thermocapillarity.

IV. TRAVELING WAVE SOLUTIONS

Experiments have shown steadily propagating droplet or beadlike solutions separated by long gaps of constant radius [8]. In this subsection, we will examine the influence of effect of thermocapillarity on the structures of traveling wave solutions. We solve the governing equations by moving to a traveling wave coordinate, $\xi = z - ct$, where c is a constant wave speed to be determined. The nonlinear equation (34)
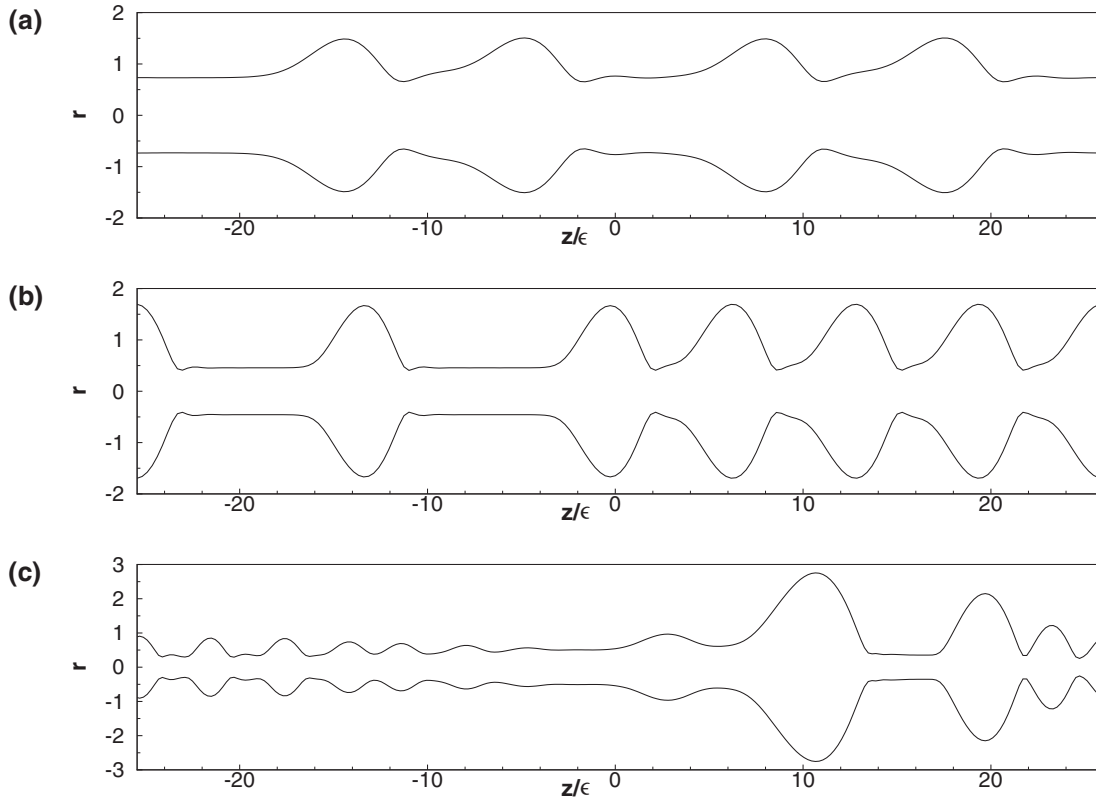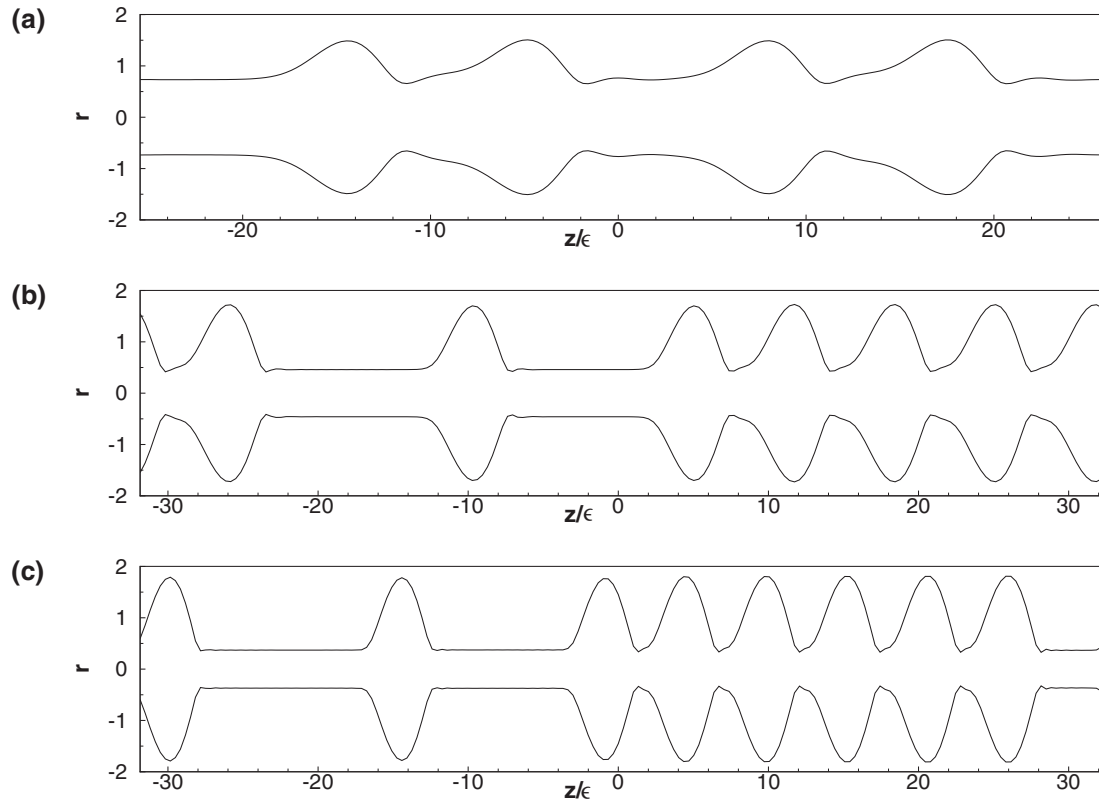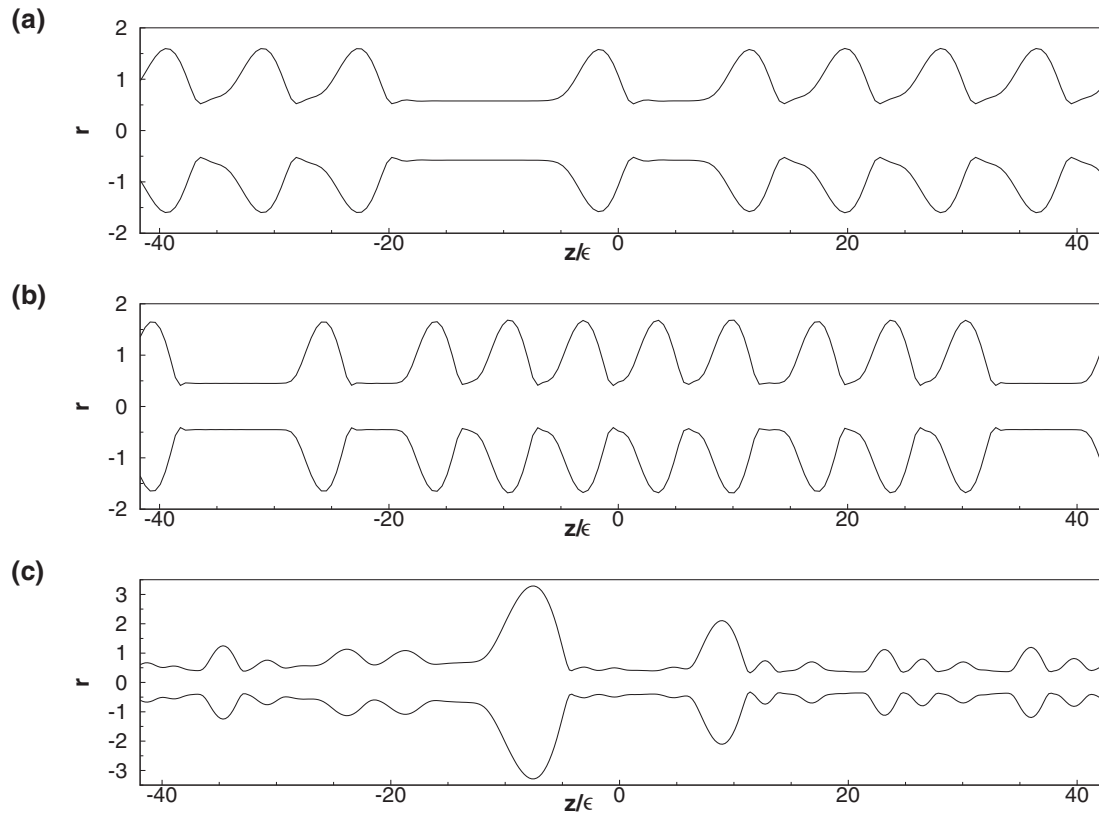
(a)

(b)

(c)

FIG. 6. The profiles of the interface via transient numerical simulations for various Marangoni numbers. Other parameters are $l = 15$, $a = 0.2551$, $\epsilon = 0.2915$. Ma $= 0, 1, 2$ for (a), (b), and (c).

(a)

(b)

(c)

FIG. 7. The profiles of the interface via transient numerical simulations for various Marangoni numbers. Other parameters are $l = 15$, $a = 0.2856$, $\epsilon = 0.233$. Ma $= 0, 1, 2$ for (a), (b), and (c).

(a)

(b)

(c)

FIG. 8. The profiles of the interface via transient numerical simulations for various Marangoni numbers. Other parameters are $l = 15$, $a = 0.3262$, $\epsilon = 0.178$. Ma $= 0, 1, 2$ for (a), (b), and (c).
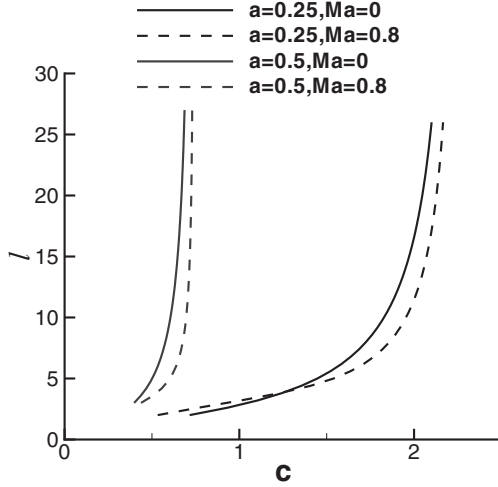
FIG. 9. Traveling wave solution: spacings l and propagating speeds c for various a and Ma at $\epsilon = 0.2$.

becomes

$$-c\partial_\xi S^2 + 2\partial_\xi Q(S) = 0. \tag{43}$$

Integrating this equation, we have

$$-cS^2 + 2Q(S) = q. \tag{44}$$

Equation (44) subject to periodic boundary conditions will be solved in the region of $-l/2 < \xi \leqslant l/2$, where l is the length of the computational domain. In order to fix c, we impose a constraint condition on the fluid mass:

$$\int_{-l/2}^{l/2} (S^2(\xi) - a^2)d\xi = l(1 - a^2). \tag{45}$$

Equation (44) becomes a nonlinear differential eigenvalue problem where the unknown variables are the fluid radius $S(\xi)$, q, and c.

A Newton-Kantorovich approach with a Fourier expansion is used to solve the nonlinear eigenvalue problem. We begin with a reasonable guess obtained from direct simulation for the wave speed c and profile $S(\xi)$. The traveling wave solution can be rapidly converged via Newton iterations. We should note that the steadily propagating solution may be obtained by direct simulation on the initial problem. For each point in the curve, an independent simulation is needed. The procedures are highly time consuming.
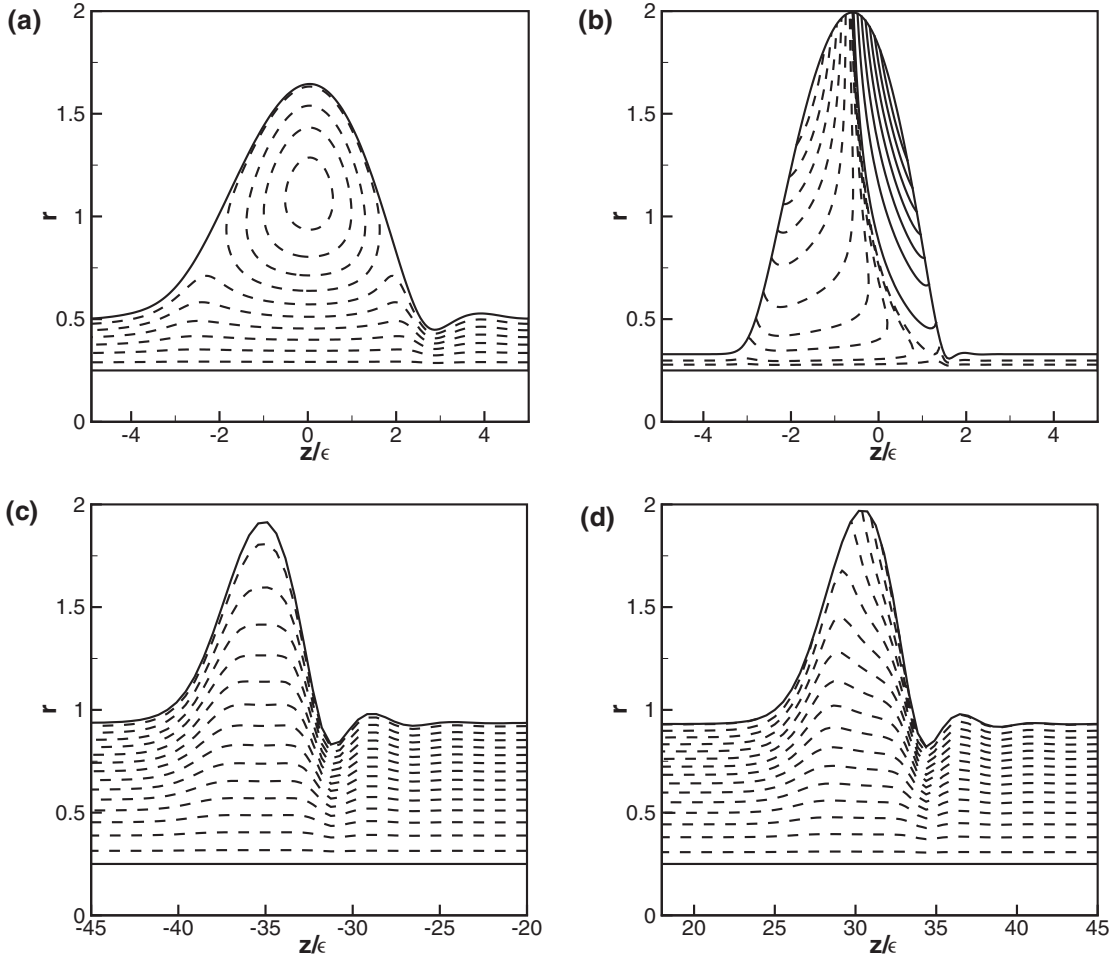

FIG. 10. The profiles of the interface and the isostreamlines for $a = 0.25$. Other parameters are (a) Ma = 0, $l = 2$, (b) Ma = 0.8, $l = 2$, (c) Ma = 0, $l = 20$, (d) Ma = 0.8, $l = 20$. Negative and positive values of the stream function are denoted by dashed and solid lines.
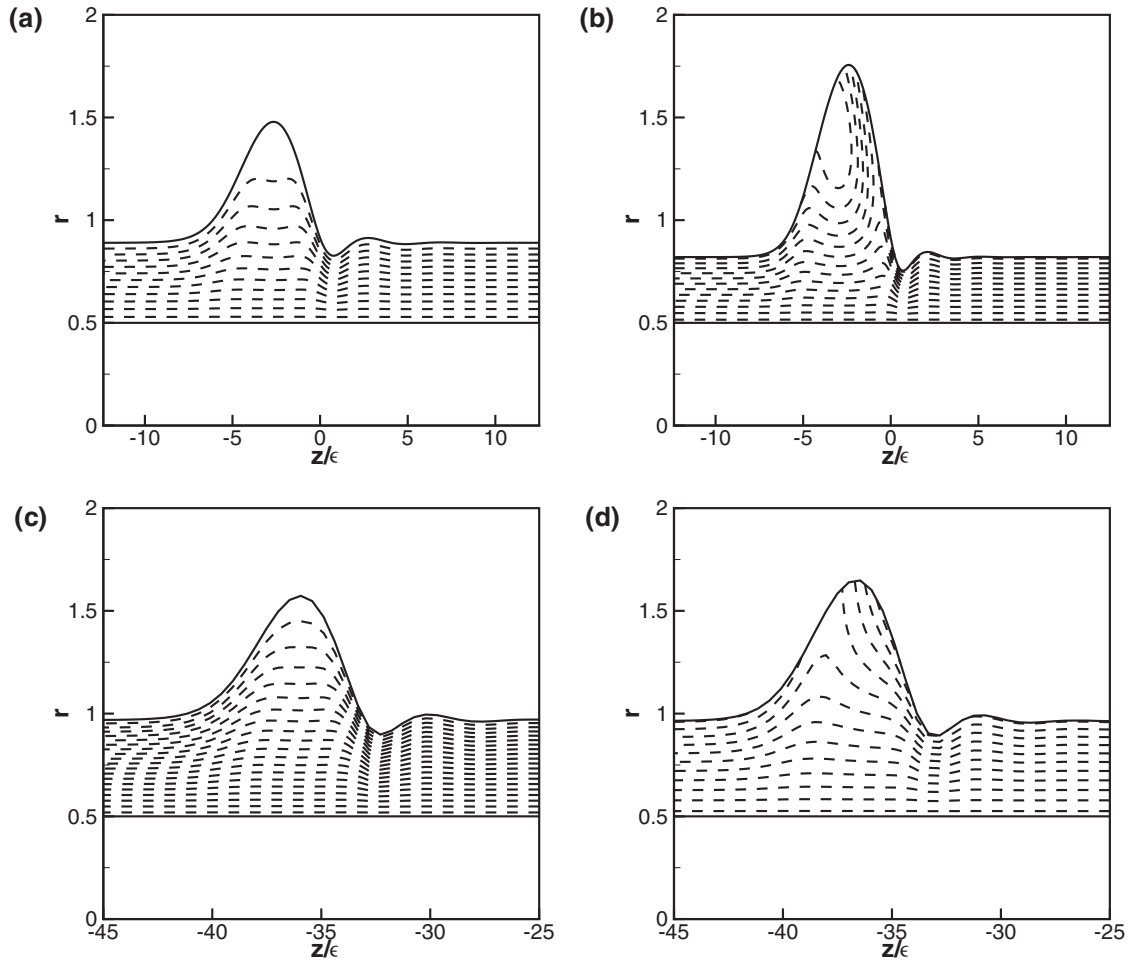
FIG. 11. The profiles of the interface and the isostreamlines for $a = 0.5$. Other parameters are (a) Ma $= 0$, $l = 5$, (b) Ma $= 0.8$, $l = 5$, (c) Ma $= 0$, $l = 20$, (d) Ma $= 0.8$, $l = 20$. Negative values are denoted by dashed lines.

Figure 9 displays the variation of the wave speed c with the domain length l for various a and Ma. In this figure the structure of each curve is similar, i.e. the solutions with smaller l travel slower than those with larger l. This implies that the droplets of relatively long waves eventually catch up with, coalesce and consume those of shorter wavelength. The wave speed c asymptotes to a certain value, c_∞, as l increases to a large value. For a given l, it is clear that the wave speed of $a = 0.5$ is much lower than that of $a = 0.25$. This means that the thinner layer of fluid gives rise to droplets propagating more slowly than that of the thicker layer. Comparing the curves of Ma $= 0$ with Ma $= 0.8$ for $a = 0.5$, we found that with the increase of Ma the droplets propagate faster for almost all values of l. Comparing the curves of Ma $= 0$ with Ma $= 0.8$ for $a = 0.25$, at small l the wave speed of Ma $= 0$ is faster than that of Ma $= 0.8$. However, at large l the wave speed of Ma $= 0$ is slower than that of Ma $= 0.8$.

In order to know more about the influence of thermocapillarity on the traveling wave solution, we plot the structures of the streamlines of the traveling waves in the moving frame of reference for several cases in Figs. 10 and 11. In Fig. 10, the figures of the case of $a = 0.25$ are presented for various wavelengths and Marangoni numbers. In each figure, the

dashed lines indicate that in the moving frame the fluid moves upwards underneath the waves. In Fig. 10(a) for $l = 2$, at Ma $= 0$ the maximum height of the film is about 1.7. A small capillary ripple exists in the region wherein the droplet adjusts onto the preceding flat region. The thickness of the gap region varies smoothly. As shown in Fig. 10(b), the increase of Ma results in a more pronounced peak with the height of about 2 and a less pronounced adjustment region. As Ma increases from 0 to 0.8, the thickness of gap region decreases from about 0.25 to 0.06. As shown in Fig. 10(a) for Ma $= 0$, the streamlines in the moving frame reveal a large recirculation zone inside the bead. For Ma $= 0.8$, the structure of the streamlines is significantly different from that in Fig. 10(a). In Fig. 10(b), two circulations rotating in opposite directions are formed under the Marangoni effect. The streamlines in Fig. 10(b) reveal that fluid particles move from the peak into inner region of the bead.

For $l = 20$, in Figs. 10(c) and 10(d) the traveling wave solutions are in the form of pulse-like waves. In each figure the negative isostreamlines indicate that in the moving frame the fluid moves upwards underneath the waves. The height of the peak slightly increases with the increase of Ma. In Figs. 10(c) and 10(d), there is no circulation inside the beads for both

cases. For Ma = 0.8, the streamlines in Fig. 10(d) show that near the peak region there are fluid particles flowing from the interface into the bead.

In Fig. 11 we plot the profiles of the interface and streamlines for the case of $a = 0.5$ for various Ma and l. In each figures, a noticeable capillary ripples present in front of the beads. Comparing Fig. 11(a) with 11(b) and Fig. 11(c) with 11(d), we found that the increase of Ma results in the increase of the height of the beads. In Fig. 11(a) and 11(c) for $l = 5$ and 20, in the absence of the Marangoni effect there is no circulation inside the beads, and there are no fluid particles flowing from the interface into the beads. However, for Ma = 0.8 as shown in Figs. 11(b) and 11(d) there are fluid particles flowing from the interface into the beads.

V. CONCLUSIONS

This paper investigates the dynamics of a fiber flow driven by the gravity combined with thermocapillarity induced by a temperature gradient in the radial direction. The evolution equation for the interface is obtained via long-wave theory. The parameters a, ϵ, Ma, and Bi are involved in the evolution equation.

We studied the linear stability of small axisymetric disturbances. We focus on the Marangoni effect on the stability of the fiber flow. The results show that both the time growth rate and the wave number of the most unstable mode increase with the increase of Ma. This means that the Marangoni effect and the Rayleigh-Plateau mechanism reinforce each other.

We performed numerical simulations on the nonlinear evolutions of most unstable disturbance. At the saturate state of the most unstable disturbances, with the increase of Ma the heights of the beads increase and the gap between the beads becomes flatter and the thickness of the gap decreases. We also performed a transient simulations of random small disturbances over relatively long flow region. In the absence of thermocapillarity, the structures of the profiles of the interface of flow regime (a), (b), (c) are noticeably different. However, with the increase of Ma, the profile of the interface consists of series of smaller beads. As Ma increases further, the thicknesses of the gap between the beads decrease and breakup of the interface may occur. The results of the transient simulations show that with the increase of Ma the fiber flow has a tendency to breakup into smaller droplets.

The traveling wave solutions are investigated by a Newton-Kantorovich approach. The results show that the solutions with smaller l travel slower than those with larger l. This implies that the droplets of relatively long waves eventually catch up with, coalesce and consume those of shorter wavelength. For smaller a, with the increase of Ma the droplets propagate faster for almost all values of l. For larger a, at small l the wave speed decreases with Ma. However, at large l the wave speed increases with Ma.

[1] D. Quéré, Annu. Rev. Fluid Mech. **31**, 347 (1999).

[2] L. Rayleigh, Phil. Mag. **34**, 145 (1892).

[3] D. Quéré, Europhys. Lett. **13**, 721 (1990).

[4] A. L. Frenkel, Europhys. Lett. **18**, 583 (1992).

[5] S. Kalliadasis and H.-C. Chang, J. Fluid Mech. **261**, 135 (1994).

[6] V. I. Kerchman and A. L. Frenkel, Theoret. Comput. Fluid Dynamics **6**, 235 (1994).

[7] H.-C. Chang and E. A. Demekhin, J. Fluid Mech. **380**, 233 (1999).

[8] I. L. Kliakhandler, S. H. Davis, and S. G. Bankoff, J. Fluid Mech. **429**, 381 (2001).

[9] R. V. Craster and O. K. Matar, J. Fluid Mech. **553**, 85 (2006).

[10] Z. J. Ding and Q. S. Liu, Phys. Rev. E **84**, 046307 (2011).

[11] Z. J. Ding, J. L. Xie, T. N. Wong, and R. Liu, J. Fluid Mech. **752**, 66 (2014).

[12] M. Sweetland and J. H. Lienhard, Int. J. Heat Mass Trans. **43**, 777 (2000).

[13] D. A. Goussis and R. E. Kelly, Int. J. Heat Mass Trans. **33**, 2237 (1990).

[14] H. Bénard, Rev. Gén. Sci. Pure Appl. **11**, 1261, (1990); **11**, 1309 (1990).

[15] M. J. Block, Nature (London) **178**, 650 (1956).

[16] J. R. A. Pearson, J. Fluid Mech. **4**, 489 (1958).

[17] L. E. Scriven, and C. V. Sternling, J. Fluid Mech. **19**, 321 (1964).

[18] K. A. Smith, J. Fluid Mech. **24**, 401 (1966).

[19] S. J. VanHook, M. F. Schatz, W. D. McCormick, J. B. Swift, and H. L. Swinney, Phys. Rev. Lett. **75**, 4397 (1995).

[20] S. J. VanHook, M. F. Schatz, J. B. Swift, W. D. McCormick, and H. L. Swinney, J. Fluid Mech. **345**, 45 (1997).

[21] J.-J. Xu and S. H. Davis, J. Fluid Mech. **161**, 1 (1985).

[22] Y.-J. Chen, R. Abbaschian and P. H. Steen, J. Fluid Mech. **485**, 97 (2003).

[23] P. Colinet, J. C. Legros, and M. G. Velarde, *Nonlinear Dynamics of Surface-Tension-Driven Instabilities* (Wiley-VCH Verlag, 2001).